ARTICLE   OPEN

Check for updates

All inkjet-printed electronics based on electrochemically exfoliated two-dimensional metal, semiconductor, and dielectric

Okin Song[1,5], Dongjoon Rhee [1,5], Jihyun Kim[1], Youngseo Jeon[1], Vlastimil Mazánek[2], Aljoscha Söll[2], Yonghyun Albert Kwon[3], Jeong Ho Cho[3], Yong-Hoon Kim[1], Zdeněk Sofer [2] and Joohoon Kang [1,4 ✉]

Inkjet printing is a cost-effective and scalable way to assemble colloidal materials into desired patterns in a vacuum- and lithography-free manner. Two-dimensional (2D) nanosheets are a promising material category for printed electronics because of their compatibility with solution processing for stable ink formulations as well as a wide range of electronic types from metal, semiconductor to insulator. Furthermore, their dangling bond-free surface enables atomically thin, electronically-active thin films with van der Waals contacts which significantly reduce the junction resistance. Here, we demonstrate all inkjet-printed thin-film transistors consisting of electrochemically exfoliated graphene, MoS_2, and HfO_2 as metallic electrodes, a semiconducting channel, and a high-k dielectric layer, respectively. In particular, the HfO_2 dielectric layer is prepared via two-step; electrochemical exfoliation of semiconducting HfS_2 followed by a thermal oxidation process to overcome the incompatibility of electrochemical exfoliation with insulating crystals. Consequently, all inkjet-printed 2D nanosheets with various electronic types enable high-performance, thin-film transistors which demonstrate field-effect mobilities and current on/off ratios of $\sim 10 \, cm^2 \, V^{-1} \, s^{-1}$ and $>10^5$, respectively, at low operating voltage.

INTRODUCTION

Solution-phase printing is driving advances in the low-cost, scalable fabrication of electronic devices, which has been difficult with conventional microfabrication techniques involving photo-lithography, vacuum deposition, and lift-off processes[1–3]. Among various printing strategies, inkjet printing has received great attention because this method can assemble functional materials into customizable patterns on various substrates in a lithography-free manner[4]. Printable ink consists of materials with desired electronic properties either dissolved or dispersed in a solvent that enables handling of the active components. By printing conducting (electrodes), semiconducting (channels), and insulating (dielectric layers) inks as building blocks, a wide range of electronic devices, including field-effect transistors (FETs), photo-detectors, light-emitting diodes, and solar cells have been demonstrated with minimal material waste[5–9]. Early work on printed electronics focused on inks based on organic molecules or polymers, but the resulting devices show limited performance compared to conventional silicon-based electronics[5,6,10]. Alternatively, inorganic materials such as metal oxides have been synthesized from precursor inks and achieved high-performance printed electronics[11–13]. In particular, a combination of inkjet-printed sol-gel metal oxide films (e.g. electrode: aluminum-doped cadmium oxide, semiconductor: indium oxide, dielectric: aluminum oxide) realized FETs with outstanding device performance with field-effect mobility of 11–230 $cm^2 \, V^{-1} s^{-1}$ and current on/off ratios $>10^{7,11,14–17}$. One drawback of this approach is that suppressing the formation of secondary phases is not trivial during the chemical conversion of the precursor film into the final

product[11]. Alternatively, the liquid metal printing strategy can form high-quality metal oxide thin films (mobilities of 14–67 $cm^2 \, V^{-1} \, s^{-1}$ and on/off ratio $>10^6$) with a more facile processing step, but the library of available materials is somewhat limited[18–20]. Recently, low-dimensional nanomaterials, including zero-dimensional (0D) nanoparticles and one-dimensional (1D) nanotubes and nanowires have been extensively investigated for high-performance printed electronics[21–24]. When these materials are assembled into thin films, however, the network exhibits electrical properties inferior to those of individual constituents because the charge transport is significantly impeded by interfacial dangling bonds and junctions[25–27].

Two-dimensional (2D) nanosheets have emerged as a promising class of ink materials because of their unique electronic properties and dangling bond-free interfaces[28]. During printing, the nanosheets are assembled into continuous films by partially stacking on top of each other. Neighboring nanosheets can, in principle, conformally overlap to form atomically clean van der Waals interfaces over large areas, which allows for drastically reduced junction resistances compared to 0D and 1D material networks[27,29]. Moreover, nanosheets with various electronic types are available in high crystalline quality via exfoliation of a family of van der Waals crystals, which circumvents the need for extra crystallization of the nanosheet film, unlike the case for the sol-gel approach. Since the successful development of stable graphene inks for printed electrodes[30–32], 2D material inks with other electronic properties, such as transition metal dichalcogenides (TMDCs) and hexagonal boron nitride (h-BN), have been demonstrated[33–35]. For scalable production of semiconductor inks, liquid-

[1]School of Advanced Materials Science and Engineering, Sungkyunkwan University (SKKU), Suwon 16419, Republic of Korea. [2]Department of Inorganic Chemistry, University of Chemistry and Technology Prague, Technicka 5, 166 28 Prague 6, Czech Republic. [3]Department of Chemical and Biomolecular Engineering, Yonsei University, Seoul 03722, Republic of Korea. [4]KIST-SKKU Carbon-Neutral Research Center, Sungkyunkwan University (SKKU), Suwon 16419, Republic of Korea. [5]These authors contributed equally: Okin Song, Dongjoon Rhee. ✉email: joohoon@skku.edu

phase exfoliation of molybdenum disulfide (MoS_2) assisted by ultrasonication has been most intensively used[33,36,37]. A major drawback of this strategy, however, is that the resulting nanosheets exhibit small lateral sizes (typically less than 100 nm) and polydispersity in thickness. As a result, printed nanosheets are not closely aligned along the in-plane direction and are connected mostly by edge-to-edge with little overlap[38,39]. This porous network structure exhibits large junction resistances, and hence the carrier mobility is highly limited ($<0.01\ cm^2\ V^{-1}\ s^{-1}$)[36,40]. Recently, the electrochemical exfoliation process using molecular intercalants has been developed to mass produce few-layered MoS_2 nanosheets with large lateral sizes ($>1\ \mu m$), which enables large-area, conformal junctions between nanosheets[29]. Although a significant improvement in field-effect mobility was possible ($0.1\ cm^2\ V^{-1}\ s^{-1}$) by inkjet printing of the electrochemically exfoliated MoS_2 ink[41,42], the electrical performance is still far below the prototype device based on a single MoS_2 microflake from micromechanical exfoliation (mobility of $\sim200\ cm^2\ V^{-1}\ s^{-1}$)[43]. Furthermore, the photoresponsivity of the 2D semiconductors is still limited, which hinders their application in photodetectors[37,44–48].

Besides the high-quality semiconducting channels, sub-10-nm high-dielectric-constant (high-k) insulating films are also essential to achieve high field-effect mobility and low operating voltage[49,50]. Dielectric layers most commonly used for high-performance inkjet-printed FETs are based on metal oxides such as aluminum oxides or zirconium oxides, which can achieve $k > 20$[15,17]. Although these high-k materials are already well established, developing 2D-material-based high-k dielectrics is potentially advantageous for enhancing the performance of 2D semiconductor devices because they can form atomically flat, dangling bond-free interfaces with minimal charge transport losses[34]. Printed 2D dielectric layers are mostly based on h-BN nanosheets that are produced *via* liquid-phase exfoliation because the electrochemical exfoliation method is not directly applicable to produce intrinsically insulating materials[38,51–54]. The resulting liquid-phase exfoliated dielectric samples with small lateral size and polydisperse thickness distribution can be limited to form pinhole-free percolating networks in sub-10-nm scale thickness; instead, the film thickness needed to be several micrometers to minimize leakage currents, resulting in low areal capacitances ($<10\ nF\ cm^{-2}$)[51–53]. Furthermore, the dielectric constant of the h-BN crystal ($k \approx 5$) is much lower than conventional high-k dielectric materials such as HfO_2 ($k \approx 25$) and Al_2O_3 ($k \approx 9$)[55,56]. The development of new high-k 2D nanosheet ink materials that can be processed into nanometer scale thin films without pinholes will be highly beneficial to realize high-performance printed electronics.

Here, we present inkjet-printed electronics in which all the device building blocks consist of solution-processed 2D nanosheets. Molecular intercalation-assisted electrochemical exfoliation process was used to produce graphene, MoS_2, and HfS_2 nanosheets with large lateral sizes that are stabilized in alcohol-based solvents. Without the addition of surfactants or additives, the inks could be printed to form uniform, nanoscale thin films without coffee-ring features or residues. Semiconducting channels from inkjet-printed MoS_2 showed superior electrical properties and photoresponsivity with high spatial uniformity because the nanosheets are well-aligned along the in-plane direction. Furthermore, ultrathin (~10 nm), a high-k dielectric layer could be realized without pinholes by inkjet printing the HfS_2 nanosheet ink followed by the conversion into HfO_2 via annealing. Combining oxidized HfS_2 film as gate dielectrics, MoS_2 as channels, and graphene as electrodes, all inkjet-printed FETs were realized with the field-effect mobility ($\sim10\ cm^2\ V^{-1}\ s^{-1}$) and on/off ratio ($>10^5$) much higher than previously reported devices based on printed 2D semiconducting channels.

RESULTS

Two-dimensional nanosheet inks for all printed electronic devices

Figure 1a illustrates the atomic structure of our 2D nanosheets that can be assembled to form thin-film electronic devices exclusively by inkjet printing. Based on molecular intercalation-assisted electrochemical exfoliation of van der Waals crystals, we produced 2D nanosheets with the full range of electronic properties, including graphene as a metal, MoS_2 as a semiconductor, and oxidized HfS_2 (HfO_2) as an insulator. The exfoliated 2D nanosheets were dispersed into alcohol-based solvents, which are beneficial for the printing process because of their good wettability with the substrate and fast drying time[28,57]. The inks were then sequentially printed on a heavily doped (p^{++}) Si wafer to fabricate electronic devices, including FETs and photodetectors (Fig. 1b). Figure 1c shows optical images of the inks where 2D nanosheets are stably dispersed without aggregation. The corresponding optical absorbance spectra are also shown in Supplementary Fig. 1. Besides the stability against aggregation, rheological properties such as surface tension and viscosity are also important parameters for jetting of the ink without clogging the nozzle or formation of satellite droplets[58]. Based on the measured surface tension (γ), viscosity (η), and density (ρ) of the ink and the nozzle diameter (a), we calculated the inverse Ohnesorge number (Z) as a figure of merit to determine the compatibility of our inks with inkjet printing.

$$Z = \sqrt{\gamma \rho a}/\eta \qquad (1)$$

The Z values of the inks were 16 for MoS_2, 21 for graphene, and 22 for HfS_2 (Supplementary Table 1), which were comparable to those of previously reported 2D material dispersions with stable inkjet printing[59–62]. A cross-sectional high-resolution transmission electron microscope (TEM) image of the printed device shows conformal stacking of the nanosheets with a high fraction of areas that exhibit nearly identical interlayer stacking with that of the original van der Waals crystals (Fig. 1d). This superior stacking morphology is critical to promote charge transport within 2D nanosheet building blocks and enhance the device performance of the van der Waals heterostructures.

MoS_2 nanosheet ink from electrochemical exfoliation using molecular intercalants

Figure 2a illustrates the process for producing two-dimensional (2D) MoS_2 nanosheet inks by applying molecular intercalation-assisted electrochemical exfoliation. A MoS_2 crystal was loaded into a two-electrode electrochemical cell with a tetraheptylam-monium bromide (THAB) electrolyte, followed by the application of a voltage to intercalate THA^+ ions in between the MoS_2 layers (Methods). Then, the MoS_2 nanosheets were separated by breaking the van der Waals bonds between the intercalated layers using mild sonication and dispersed in isopropyl alcohol (IPA) to form a stable ink. Based on the atomic force microscopy (AFM) analysis (Fig. 2b, c and Supplementary Fig. 2), we found that the MoS_2 flakes are mostly 1–2 layers thick with an average lateral size of 1 μm. The presence of MoS_2 was also confirmed by the Raman spectrum (Fig. 2d), in which E^1_{2g} (in-plane vibration) and A_{1g} (out-of-plane vibration) peaks were located at 381 and 405 cm^{-1}, respectively. The peak separation and the intensity ratio (A_{1g} peak intensity divided by E^1_{2g} peak intensity) were 24 cm^{-1} and 1.4, respectively, which are in reasonable agreement with the few-layer MoS_2[63]. Fig. 2e shows representative strobo-scopic images of the MoS_2 droplet morphology at different times during printing. Although we used MoS_2 nanosheets with much larger lateral sizes compared to previous work on inkjet printing[36–38,57,60,61], the ink could be jetted to form a single droplet (30 μm in diameter) without satellite droplets $\sim160\ \mu s$
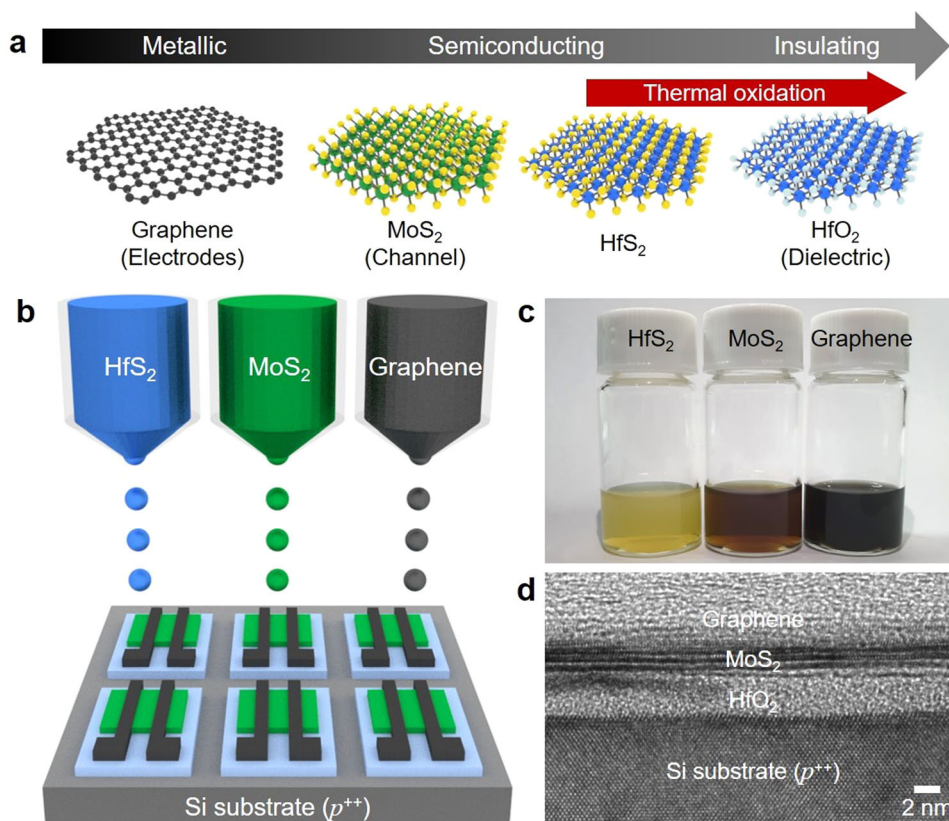
Fig. 1 All inkjet-printed thin-film electronics based on two-dimensional materials. a Atomic structures and electronic properties of the ink materials, including metallic graphene, semiconducting MoS$_2$, and insulating HfO$_2$ (oxidized HfS$_2$). **b** Schematic illustration of the inkjet printing process. **c** Optical image of the inks, where MoS$_2$ and HfS$_2$ are dispersed in isopropanol (0.5 mg mL^{-1}) and graphene are dispersed in ethanol/DMF binary solvent (10:1 volume ratio) (0.5 mg mL^{-1}). **d** Cross-sectional transmission electron microscope (TEM) image of the all inkjet-printed transistor.

after jetting. During drying on the surface, the ink droplet forms a spherical-cap shape and evaporates faster at the periphery. This geometry generates radially outward capillary flows, which often result in nanosheet transport to the droplet edges to form coffee-ring features[64–67]. We investigated IPA-based solvents with different compositions to test whether we can suppress the coffee-ring effect by adjusting solvent characteristics. Figure 2f–i shows the surface topography of the inkjet-printed MoS$_2$ films resulting from IPA/2-butanol binary mixtures with different volume ratios. The film uniformity improved by decreasing the 2-butanol content; notably, the ink with 100% IPA produced uniform films without coffee-ring features. This trend can be explained by differences in the evaporation rates of the solvents. We believe that the nanosheet transport by capillary flow could be greatly suppressed for 100% IPA because the solvent evaporates most rapidly, whereas the addition of 2-butanol slowed down the solvent evaporation and the capillary-driven outward transport became more pronounced[66,68].

Electronic properties of inkjet-printed semiconducting MoS$_2$ channels

To investigate the fidelity of inkjet printing, we printed the MoS$_2$ ink into various microscale patterns, including dot and crossbar arrays on 300-nm SiO$_2$/Si substrates. Based on the relation between solvent composition and film topography (Fig. 2f–i), 100% IPA were used as an optimized ink formulation. The morphology of the resulting patterns was investigated based on the optical microscope and scanning electron microscope (SEM) images (Fig. 3a). In particular, the MoS$_2$ microdot array consists of periodic dots with a diameter of 50 µm that are arranged in a square lattice with a periodicity (center-to-center distance between adjacent dots) of 200 µm. The crossbar array was realized by printing two arrays of MoS$_2$ line features with the lines aligned perpendicular to each other. Each array exhibits a line width of 55 µm and a periodicity (center-to-center distance between adjacent lines) of 200 µm therefore, the overlapping regions form an array of squares with a square width of 55 µm and periodicity of 200 µm. Only with one printing pass, both MoS$_2$ microdot and crossbar arrays show uniform dense films without coffee-ring features. Spatial mapping of photoluminescence (PL) peak intensity from the MoS$_2$-printed substrate further confirms that the ink can be printed into desired patterns with high fidelity without coffee-ring effects and residual features (Fig. 3b). With the ability to assemble MoS$_2$ nanosheets into desired patterns, we investigated charge transport mechanisms in the MoS$_2$ film by analyzing temperature-dependent current-voltage characteristics of a channel printed into a rectangular shape (length: 20 µm, width: 165 µm, thickness: 18 nm) (Fig. 3c). The MoS$_2$ film was treated with a bis(trifluoromethane)sulfonimide (TFSI) solution to passivate the sulfur vacancies and reduce unintentional doping[29,69], followed by deposition of Cr/Au electrodes for electrical contacts. Figure 3d shows the current-voltage curves measured at different temperatures ranging from 150.15 K to 300.15 K, where the current level increases with increasing temperature. From the current measurements, electrical conductivities (σ) were determined to reveal the dominant mechanisms for charge transport within the MoS$_2$ nanosheet film (Fig. 3e).
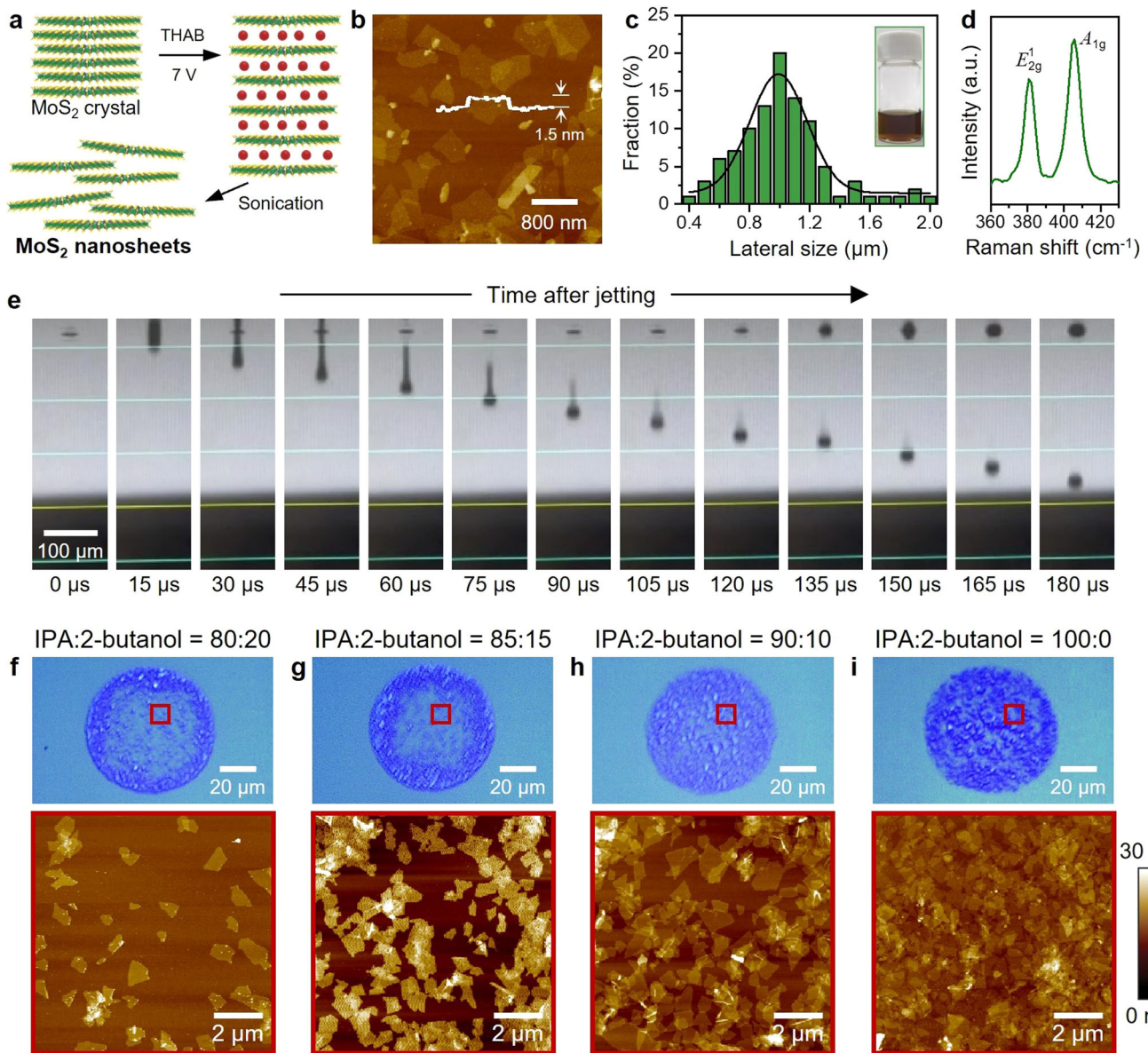
$$\sigma = \frac{L}{W \cdot t} \frac{I_D}{V_D} \tag{2}$$

Fig. 2 MoS₂ nanosheet ink produced via electrochemical exfoliation using molecular intercalants. a Schematic illustration of the electrochemical exfoliation process. **b** Atomic force microscope (AFM) image of the exfoliated MoS₂ nanosheets. White line in the image shows the height profile. **c** Histogram showing the lateral size distribution of the MoS₂ nanosheets. **d** Raman spectrum of the MoS₂ nanosheet film measured with a 532 nm laser. **e** Stroboscopic images showing the time evolution of the MoS₂ droplet morphology after jetting. **f–i** Optical microscope and AFM images of dot-patterned MoS₂ films (diameter: 70 μm) resulting from different ink formulations. One printing pass was used.

where L, W, and t are the channel length, width, and thickness, respectively, I_D is the drain current, and V_D is the drain voltage[42]. Because the MoS₂ film consists of randomly oriented nanosheets that are connected by inter-sheet junctions, the system can be considered as a disordered semiconductor, where conductivity typically exhibits a characteristic temperature dependence[42,70]:

$$\ln \sigma \sim -T^{-p} \quad (3)$$

Here, T is the absolute temperature and p is an exponent that depends on the type of transport. We found that our MoS₂ network was dominated by the 2D variable range hopping (VRH) mechanism ($p = 1/3$) at low temperatures up to ~230 K, which indicates that the electrons transport mostly along the in-plane direction because nanosheets are highly aligned on the surface due to the large lateral size[70,71]. At higher temperatures

($T > 230$ K), nearest-neighbor hopping (NNH) mechanism ($p = 1$) dominated.

We further characterized the electronic properties of the printed MoS₂ based on the back-gated FET configuration. After printing an array of MoS₂ microdots on the SiO₂/Si substrate as channels, we deposited Cr/Au electrodes using photolithography (Fig. 3f). Figure 3g shows the output characteristics of a representative FET at different gate voltages. As expected for a FET, current saturation behavior was observed at high drain voltages. Also, the device was characterized by linear current-voltage curves for small drain voltages (Supplementary Fig. 3), which suggests that the contact between the MoS₂ channel and Cr/Au electrodes was Ohmic-like with a small barrier. The gate-voltage-dependent current-voltage response indicates that the inkjet printing can form semiconducting MoS₂ channels that are sufficiently thin to enable gate modulation. From the representative transfer curve
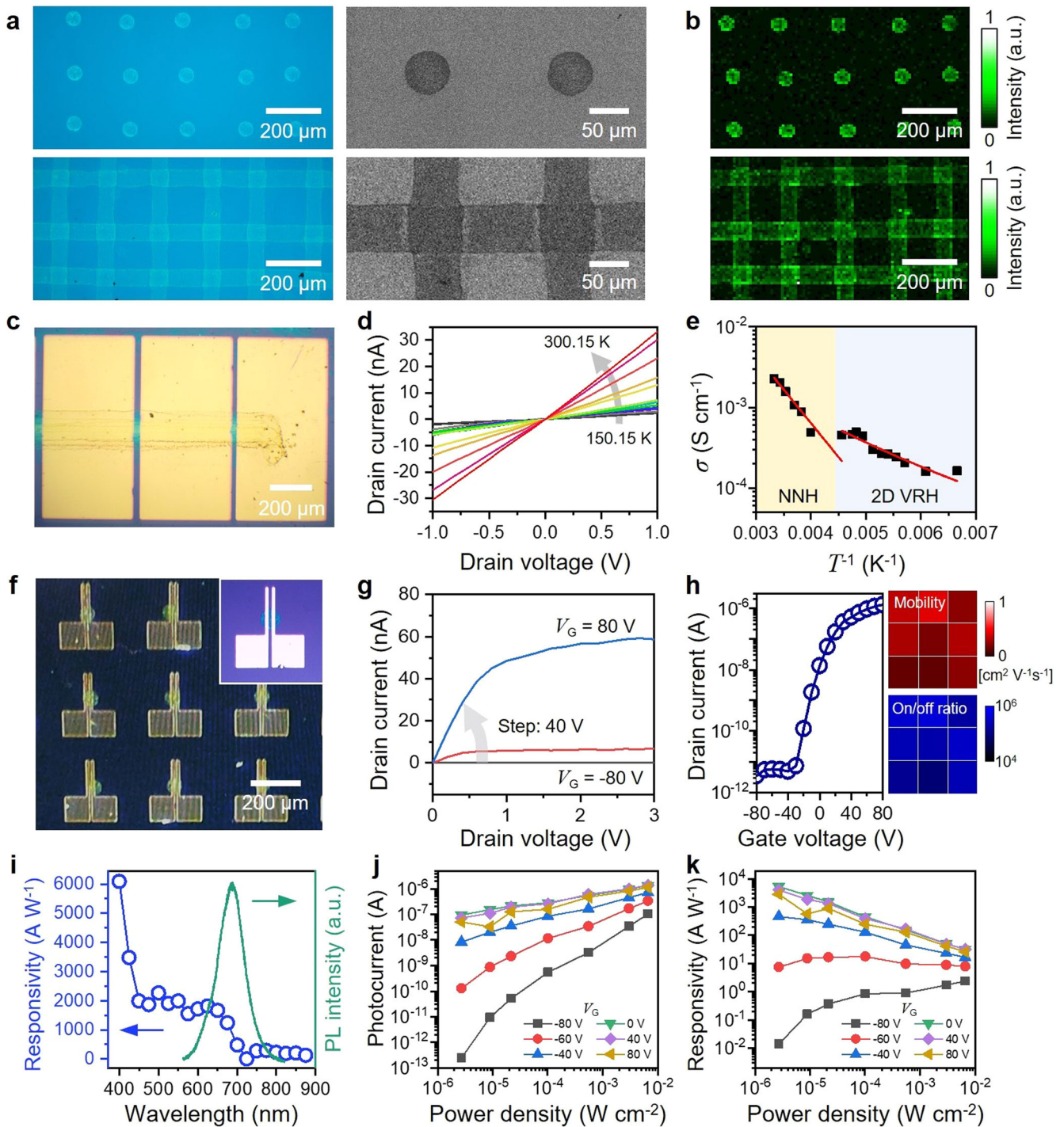
Fig. 3 Inkjet printing of semiconducting MoS₂ channels. a Optical microscope and scanning electron microscope (SEM) images of MoS₂ films are printed into different patterns. For the microdot array (one printing pass), the dot diameter and center-to-center spacing between dots were 50 and 200 µm, respectively. For the crossbar array (one printing pass for each line array), the line width and center-to-center line spacing were 55 and 200 µm, respectively. **b** Photoluminescence mapping of patterned MoS₂ films using 532-nm laser excitation. **c** Optical image of the inkjet-printed MoS₂ film (channel width: 165 µm, length: 20 µm, thickness: 18 nm) and vacuum-deposited electrodes (Cr 5 nm/Au 40 nm) for temperature-dependent conductivity measurement. **d**, **e** Current-voltage characteristics and conductivities of the MoS₂ film at different temperatures. **f** Optical image of the field-effect transistor (FET) array based on inkjet-printed MoS₂ channels (channel width: 65 µm, length: 10 µm, thickness: 18 nm) and vacuum-deposited electrodes (Cr 5 nm/Au 40 nm) on a 300-nm SiO₂/Si substrate. **g** Output characteristics. **h** Transfer curves and spatial mapping of the mobility and current on/off ratio ($V_D = 1$ V). **i** Photoresponsivities of the MoS₂ FET at different wavelengths under optical power density of ~10 µW cm⁻² ($V_D = 1$ V). Photoluminescence spectra of the MoS₂ channel is also plotted as a reference. **j**, **k** Photocurrents and photoresponsivities at different laser power densities under 520-nm laser illumination ($V_D = 1$ V).

(Fig. 3h, plot), we confirmed that the device exhibits an *n*-type behavior with a threshold voltage of ~12 V. The FET array showed a high spatial uniformity in mobility (μ) and on/off ratio (I_{on}/I_{off}) with average values of 0.24 cm^2 V^{-1} s^{-1} (standard deviation, SD: 0.094 cm^2 V^{-1} s^{-1}) and 2.4 × 10^5 (SD: 1.0 × 10^5), respectively (Fig. 3h, 2D mapping). Optoelectronic properties of the inkjet-printed MoS$_2$ film were also analyzed by characterizing the current response of the FET array under a light. Figure 3i shows the photoresponsivity (R) of a representative device (blue data) over a range of wavelengths (400–880 nm). At each wavelength, we obtained the photocurrent (I_{ph}) from the difference between the drain currents measured under light (I_{light}) and under dark conditions (I_{dark}), which was then divided by the incident optical power density (P) and the effective illumination area (S) to determine the photoresponsivity (R).

$$R = I_{ph}/PS \tag{4}$$

For wavelengths longer than 700 nm, photoresponsivity values were much smaller ($R < 300$) than those measured at shorter wavelengths because the energy of the incident photons was smaller than the bandgap of monolayer or bilayer MoS$_2$[72], which existed in a high fraction within the MoS$_2$ nanosheet population. As the excitation wavelength becomes shorter ($\lambda < 700$ nm), the device exhibited photoresponsivities higher than 1000 as the photon energy was sufficient to create photoelectrons also in the monolayer and bilayer nanosheets. Notably, we observed a characteristic peak at around 625 nm, which was close to the photoluminescence emission peak (~687 nm) resulting from the ground-state direct transition at the K point of the Brillouin zone (Fig. 3i, green line)[57]. The photoresponsivity increased with decreasing wavelength as the energy of the incident photon became higher. The inkjet-printed MoS$_2$ photodetector was further investigated at different optical power densities under 520 nm laser illumination to characterize the power-dependent photoresponse (Fig. 3j, k). As expected for a photodetector based on an *n*-type semiconducting channel, both I_{ph} and R increased when positive gate voltages were applied. From the relation between the photoresponsivity and optical power density

$$R \propto P^{\alpha-1} \tag{5}$$

we found that photocurrents were generated mostly by the photoconductive mechanism under gate voltages of −80 and −60 V because the power exponent (α) was close to 1[73,74]. The power exponent became smaller than 1 as the gate-voltage increased, which suggests that photogating effect contributed to the photocurrent generation[73,74]. The maximum photoresponsivity of ~5.2 × 10^3 A W^{-1} was achieved under illumination at a power density of 2.7 μW cm^{-2} under a gate and drain voltages of 0 and 1 V, respectively, which is higher than many of the previously reported MoS$_2$ photodetectors[37,48,75–77].

Inkjet printing of electrochemically exfoliated graphene nanosheets for electrodes

For fabrication of electrodes via inkjet printing, we produced graphene nanosheet inks from graphite based on the electrochemical exfoliation process that we used for MoS$_2$ inks, except that tetrabutylammonium hydrogen sulfate (TBAHS) molecules were used as intercalants (Fig. 4a, Methods). For stable inkjet printing, graphene nanosheets were dispersed in an ethanol/DMF mixture (10:1 volume ratio) at a concentration of 0.5 mg mL^{-1}. The representative AFM image and lateral size distribution of the resulting dispersion indicate that the solution mostly consisted of 2–3 layer graphene nanosheets with an average lateral size of 1 μm (Fig. 4b,c and Supplementary Fig. 4). The Raman spectrum showed D and G peaks located at 1360 cm^{-1} and 1620 cm^{-1}, respectively (Fig. 4d), which further confirms the presence of

graphene. To find an optimal processing condition for electrode fabrication, we investigated the surface topography and height profiles of rectangular-shaped graphene films (550 μm × 300 μm) inkjet-printed on SiO$_2$/Si substrates as a function of printing pass (Fig. 4e). The films were annealed at 300 °C to remove residual solvents and enhance the electrical properties (Supplementary Fig. 5). Note that the satellite spots in the optical microscope images (Fig. 4e) were from the initial stage of the inkjet printing process, during which some ink droplets were unintentionally deposited outside the registered pattern area. These artifacts do not affect the device characteristics and can be readily found in inkjet-printed electronic devices. As the number of printing passes increased from 1 to 30, the film became denser and connectivity between nanosheets was improved. The thickness of the film also became thicker as the number of printing passes increased, with an average thickness of ~200 nm for 30 passes. Figure 4f shows the corresponding current-voltage curves measured in a two-electrode configuration, which exhibit expected ohmic characteristics for all tested printing passes. The data plotted on a semi-logarithmic scale are also provided in Supplementary Fig. 6, which shows higher current levels for the increasing number of printing passes. From the current-voltage measurements, conductivity and sheet resistance of the graphene films could be determined (Supplementary Fig. 7 and Supplementary Table 2). As expected, the film exhibited the highest conductivity (21.7 S cm^{-1}) and lowest sheet resistance (2.2 kΩ sq^{-1}) in the case of 30 printing passes, and therefore we hereafter focused on this optimal condition for fabricating the graphene electrodes for the devices. Based on the concentration of our ink (0.5 mg mL^{-1}), we determined that the mass loading for the graphene electrode per printing pass was 1.4 × 10^{-5} mg cm^{-2}. This was the highest loading that could be achieved with our graphene ink, above which the printing nozzle started to clog because of the large lateral size of the electrochemically exfoliated graphene nanosheets. As a result, we found that our graphene electrode formed with 30 printing passes exhibited a lower conductivity (21.7 S cm^{-1}) compared to the electrode that was created with 1 printing pass of the state-of-the-art terpineol-based graphene ink (80 S cm^{-1}), in which ultrasonically exfoliated graphene nanosheets with small lateral sizes (average lateral size of ~50 nm) were dispersed at a much higher concentration (3.4 mg mL^{-1})[32]. Although the throughput of the printing process was lower compared to the case with the terpineol-based graphene dispersion, our ink could realize electrodes with sufficiently high conductivity to fabricate operating devices. Figure 4g shows FETs based on inkjet-printed graphene electrodes and MoS$_2$ channels on SiO$_2$/Si substrates (Methods). The width and length of the channel were 120 and 140 μm, respectively. Output characteristics (Fig. 4h) and transfer curves (Fig. 4i) reveal that the device exhibits an *n*-type behavior with μ and I_{on}/I_{off} of 0.02 cm^2 V^{-1} s^{-1} and 6.56 × 10^3, respectively, at a drain voltage of 1 V. Good electrical contact between the MoS$_2$ and graphene was also confirmed by the linear current-voltage behavior in the small voltage regime of the output curves (Supplementary Fig. 8). In addition to the simple rectangle-shaped patterns, the graphene electrodes could also be printed with more complex geometries that are beneficial for enhancing the device performance. As a demonstration, we realized a working MoS$_2$ photodetector with interdigitated graphene electrodes (Supplementary Fig. 9).

Inkjet-printed gate dielectrics from electrochemically exfoliated HfS$_2$ nanosheets

Finally, we produced HfS$_2$ nanosheet inks that can be converted into high-*k* dielectrics after printing and annealing. For ink formation, HfS$_2$ crystals were electrochemically exfoliated by applying the same process used for creating MoS$_2$ nanosheet inks (Fig. 5a, Methods). Figure 5b shows AFM images of the HfS$_2$
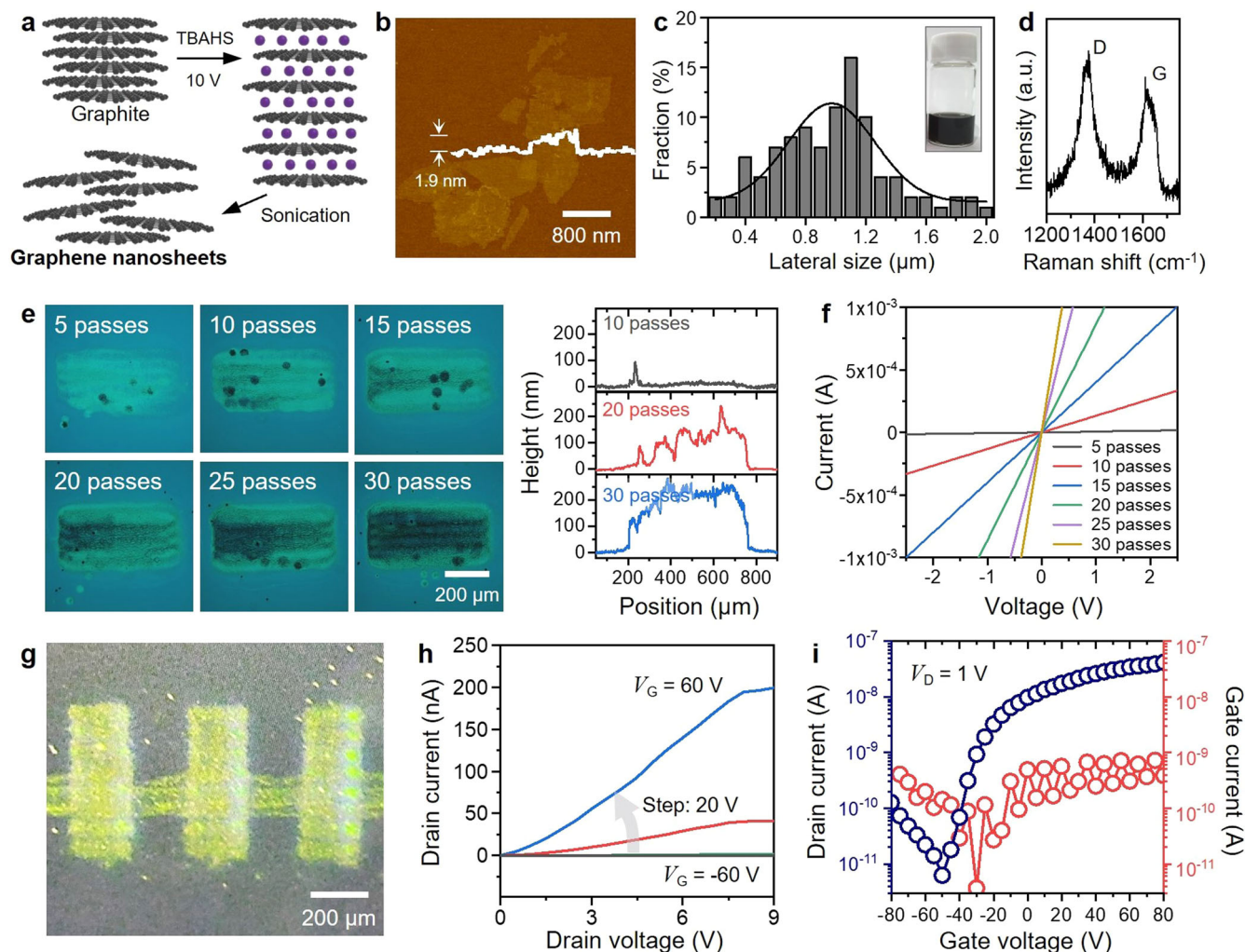
Fig. 4 Inkjet-printed electrodes based on electrochemically exfoliated graphene nanosheets. a Scheme describing the electrochemical exfoliation process. **b** AFM image of the exfoliated graphene nanosheets. White line in the image shows the height profile. **c** Histogram showing the lateral size distribution of the graphene nanosheets. **d** Raman spectrum of the graphene nanosheet film measured with a 532 nm laser. **e** Optical microscope images and height profiles of the printed graphene electrodes for different printing passes. The dimensions of the rectangular pattern were 550 μm × 300 μm. Height profiles of the graphene electrodes formed with 10, 20, and 30 printing passes are also presented. **f** Current-voltage characteristics of the printed graphene electrodes for different printing passes. A pair of rectangular metal electrodes (Cr 5 nm/Au 40 nm) were deposited with a 20-μm electrode spacing to measure the current-voltage curves from the graphene electrode. **g** Optical image of the FET based on inkjet-printed MoS_2 channels (channel width: 120 μm, length: 140 μm, thickness: 18 nm) and graphene electrodes (200 μm × 550 μm, thickness: 207 nm) on a 300-nm SiO_2/Si substrate. **h, i** Corresponding output and transfer curves.

nanosheets before (left) and after (right) annealing at 500 °C. The average thickness significantly decreased from 3 to 0.85 nm, which suggests that the HfS_2 was converted into HfO_2 because of oxidation (Supplementary Fig. 10). The lateral size of the nanosheets was characterized by an average value of 0.56 μm (Fig. 5c). The ink was then printed into a square-shaped film (2 mm × 2 mm) on a heavily doped Si substrate to reveal the chemical conversion process of the dielectric layer in more detail (Fig. 5d). The optical images show that the film became transparent under visible light after annealing, which resulted from the formation of HfO_2. The disappearance of the Raman A_{1g} peak of HfS_2 at 338 cm^{-1} also indicates the transformation of HfS_2 into HfO_2. The HfO_2 film was further analyzed by x-ray photoelectron spectroscopy to identify chemical compositions and bonding states (Fig. 5e). The presence of Hf $4d_{7/2}$, Hf $4d_{5/2}$, O 1 s peaks along with the absence of S 2p peak clearly confirms the HfO_2 formation. We then investigated the surface topography of the HfO_2 networks as a function of printing passes to identify the minimum dielectric thickness that can be achieved without

pinholes. All the films were annealed at 500 °C to ensure that HfS_2 completely oxidize into dielectrics with a minimal leakage current (Supplementary Fig. 11). Figure 5f presents AFM images of the annealed films after 4, 6, and 8 printing passes. In the case of four passes, the film exhibited many pinholes, although the nanosheet network was continuous. As expected, the number of pinholes decreased as the network became denser for increasing printing passes. Notably, a pinhole-free HfO_2 film was achieved after eight printing passes with a thickness of only 10 nm (Fig. 5f and Supplementary Fig. 12). Based on the capacitance-voltage measurement (Methods), the areal capacitance of the optimized HfO_2 layer (eight printing passes) was determined to be 425.6 nF cm^{-2}. Although the dielectric constant ($k \approx 4.8$) was noticeably lower than the value expected for a bulk HfO_2 ($k \approx 25$)[56], most likely due to the porosity of the nanosheet film, the areal capacitance was much higher than that of conventional SiO_2 (11 nF cm^{-2} for a 300-nm film) or layer-by-layer assembled sub-10-nm h-BN nanosheet films (245 nF cm^{-2})[34]. This areal capacitance is even comparable to the spin-coated HfO_2
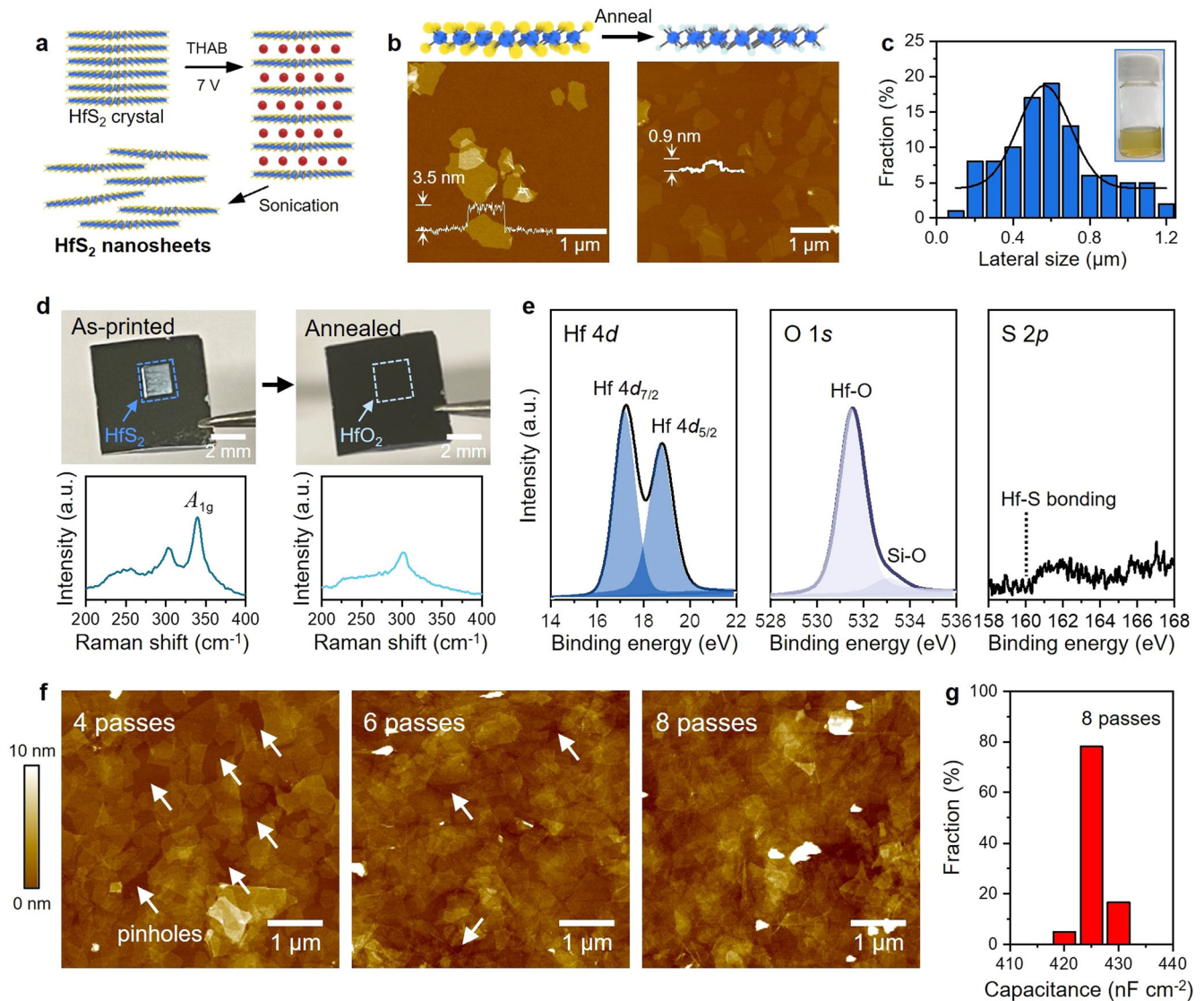
Fig. 5 **Inkjet-printed high-k dielectric based on electrochemically exfoliated HfS$_2$ nanosheets. a** Scheme describing the electrochemical exfoliation process. **b** AFM images and atomic structures of HfS$_2$ nanosheets before and after annealing. White line in the image shows the height profile. **c** Histogram showing the lateral size distribution of the HfS$_2$ nanosheets. **d** Optical images and Raman spectra (source: 532 nm laser) of the inkjet-printed HfS$_2$ (as-printed) and HfO$_2$ (annealed) films. **e** X-ray photoelectron spectroscopy (XPS) analysis of the HfO$_2$ film. **f** AFM image of inkjet-printed HfO$_2$ films formed with different printing passes. Arrows indicate pinholes. **g** Histogram showing the areal capacitance of the HfO$_2$ films for eight printing passes.

nanosheet film (519.9 nF cm^{-2}), where the film thickness could be further reduced to 3 nm without pinholes (Supplementary Fig. 13). The breakdown field of the inkjet-printed HfO$_2$ dielectric was determined to be 4.2 MV cm^{-1} (Supplementary Fig. S14).

All inkjet-printed thin-film transistors

With all the inks we developed, we fabricated FETs based on the building blocks assembled entirely by inkjet printing (Fig. 6a). HfS$_2$ was first printed on the Si substrate and annealed to create high-k HfO$_2$ dielectrics, followed by printing of MoS$_2$ channels and TFSI treatment. Graphene inks were then printed and annealed to form electrodes on top of the channels, thereby producing top-contact FETs (Methods). Figure 6b shows an SEM image of all inkjet-printed FETs along with the scheme illustrating the stacking of the building blocks. Zoomed-in SEM images of the HfO$_2$, MoS$_2$, and graphene regions are also presented in Fig. 6c. Compared to previous work on all printed 2D-material devices based on liquid-phase exfoliation[38,40,78], the surfaces appeared more uniform and smoother

with the flake edges nearly indistinguishable because the nanosheets are highly aligned along the in-plane direction. From the current-voltage measurements, we found that the printing sequence is critical for enhancing the performance of our FETs. For the case where the MoS$_2$ channels were printed after HfO$_2$ dielectric and graphene electrodes (bottom-contact FETs), we could not properly passivate the sulfur vacancies in MoS$_2$ nanosheets because graphene electrodes were affected by the TFSI treatment and the device did not show gating effects (Supplementary Fig. 15a). Although bottom-contact FETs could be fabricated without TFSI treatment, the I_{on}/I_{off} (4.7 × 10^1) was much lower compared to the TFSI-treated MoS$_2$ FETs with vacuum-deposited electrodes (Supplementary Fig. 15b and Fig. 3h). In contrast, TFSI-treated top-contact MoS$_2$ FETs exhibited the expected n-type characteristics with a clear current saturation behavior and high μ and I_{on}/I_{off} (Fig. 6d, e). The output curves in the small V_D regime also confirms that the graphene electrode and MoS$_2$ channel formed a low-resistance ohmic-like contact with a
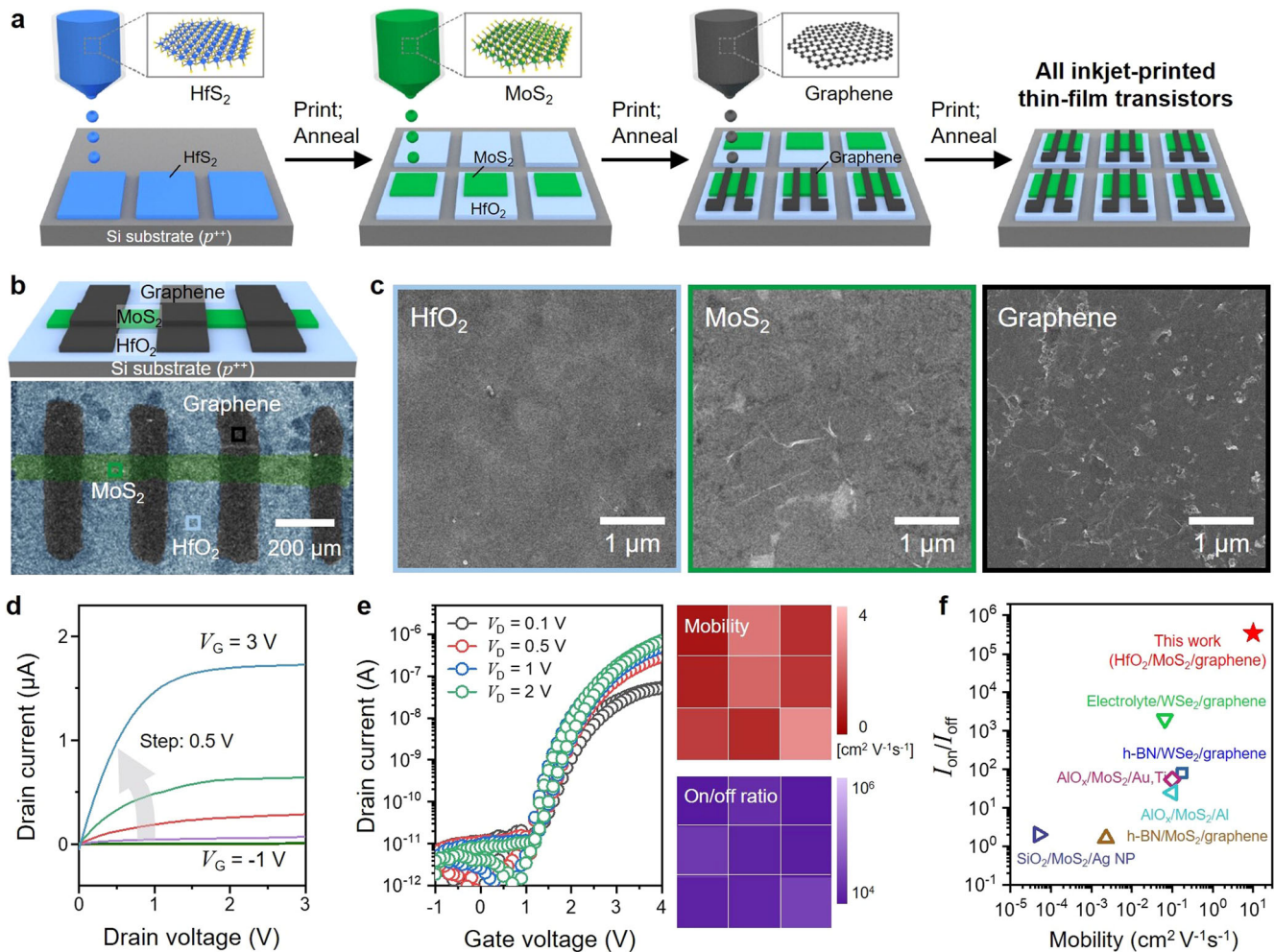
Fig. 6 All inkjet-printed field-effect transistors based on electrochemically exfoliated 2D materials. a Schematic illustration of the all inkjet-printed FET fabrication process. **b** Scheme of the resulting device and the SEM image (HfO$_2$ dielectric layer thickness: 10 nm; MoS$_2$ channel width: 100 μm, length: 170 μm, thickness: 18 nm; graphene electrode width: 130 μm, length: 530 μm, thickness: 207 nm). **c** Zoomed-in SEM images of the HfO$_2$, MoS$_2$, and graphene nanosheet films. **d, e** Output characteristics, transfer curves, and spatial mapping of the mobility and current on/off ratio of all inkjet-printed FETs. Spatial mapping was conducted at $V_D = 1$ V. The average and standard deviation values were 1.4 and 0.80 cm^2 V^{-1} s^{-1} for μ and 9.5×10^4 and 7.5×10^4 for I_{on}/I_{off}. **f** Plot comparing the mobilities and on/off ratios of FETs, where the channel was fabricated by printing 2D semiconductor nanosheets. Gate dielectric and electrodes were created either by inkjet printing, drop casting, or vacuum-phase deposition. Materials used for each device are indicated along with the data point (gate dielectric/channel/electrode). Previous work presented in the plot included SiO$_2$/MoS$_2$/Ag NP (ref. [36]), h-BN/WSe$_2$/graphene (ref. [38]), h-BN/MoS$_2$/graphene (ref. [40]), AlO$_x$/MoS$_2$/Au,Ti (ref. [41]), AlO$_x$/MoS$_2$/Al (ref. [42]), and electrolyte/WSe$_2$/graphene (ref. [79]).

minor Schottky barrier (Supplementary Fig. 16). By fabricating two independent 5×5 arrays of FETs (Supplementary Fig. 17), we found that the highest achieved μ and I_{on}/I_{off} were 10.1 cm^2 V^{-1} s^{-1} and 3.4×10^5, respectively, with the average values of 3.8 cm^2 V^{-1} s^{-1} and 1.6×10^5 at $V_D = 1$ V (array #1: average and SD were 4.2 and 1.9 cm^2 V^{-1} s^{-1} for μ and 1.2×10^5 and 8.2×10^4 for I_{on}/I_{off}; array #2: average and SD were 3.3 and 1.6 cm^2 V^{-1} s^{-1} for μ and 1.9×10^5 and 1.4×10^5 for I_{on}/I_{off}) (Supplementary Figs. 18, 19). Moreover, spatial uniformity of the transistor array performance was confirmed by spatial mappings and histograms of device metrics, including μ and I_{on}/I_{off}, as well as threshold voltage (average and SD were 1.56 and 0.084 V for array #1 and 1.51 and 0.14 V for array #2) and subthreshold swing (average and SD were 0.21 and 0.030 V dec^{-1} for array #1 and 0.24 and 0.058 V dec^{-1} for array #2) values (Supplementary Fig. 20). The μ and I_{on}/I_{off} values are much higher compared to previously reported FETs based on printed TMDC nanosheet channels (Fig. 6f)[36,38,40–42,79]. Furthermore, the device performance was even better than the TFSI-treated top-contact MoS$_2$ FETs on

spin-coated HfO$_2$ layers (average μ and I_{on}/I_{off} were 1.3 cm^2 V^{-1} s^{-1} and 9.7×10^4 at $V_D = 1$ V, while the SD values were 0.69 cm^2 V^{-1} s^{-1} and 6.1×10^4) (Supplementary Fig. 21), which highlights the benefits of our approach because inkjet printing can drastically reduce ink consumption compared to spin coating.

DISCUSSION

In summary, all inkjet-printed electronics were demonstrated by using micrometer-sized 2D nanosheets produced *via* electrochemically driven molecular intercalation and exfoliation. Metallic, semiconducting, and insulating films could be printed with uniform thicknesses without the addition of surfactants or additives. By combining the building blocks, field-effect transistors were successfully fabricated with high spatial uniformity in electrical properties and photoresponsivity, which outperforms previously reported printed 2D semiconductor-based devices. With further reduction in annealing temperature and time *via* rapid annealing processes such as photonic annealing and

through a combination strategy with other materials systems such as sol-gel metal oxide dielectrics and ultrafine graphene nanosheet conductors, we expect that this work will provide opportunities for cost-effective, scalable fabrication of high-performance wafer-scale electronics and photonic devices with high design flexibility.

METHODS

Electrochemical exfoliation of 2D materials

To prepare dispersions of MoS_2 and HfS_2 nanosheets, bulk crystals of MoS_2 (purchased from HQ graphene) and HfS_2 (synthesized by chemical vapor transport method[80]) were electrochemically exfoliated using molecular intercalants. The electrolyte was first prepared by dissolving tetraheptylammonium bromide (THAB, purchased from Sigma-Aldrich) in acetonitrile at a concentration of $5\,mg\,mL^{-1}$. After placing the crystal at the cathode and graphite at the anode, direct current was applied under 7 V for ~1 h for intercalation of THAB. The resulting crystal was then rinsed with ethanol and sonicated in a polyvinylpyrrolidone solution in dimethylformamide (DMF) (concentration: $22\,mg\,mL^{-1}$) for 30 min. To precipitate unexfoliated crystals, the solution was centrifuged at 4000 rpm for 10 min. The supernatant was then collected and washed with isopropyl alcohol (IPA) a minimum of three times to rinse residues from the nanosheets. For the preparation of graphene nanosheet dispersion, an electrochemical cell was constructed by loading graphite foils (purchased from Alfa Aesar) both into the anode and cathode. An aqueous solution of tetrabutylammonium hydrogen sulfate (TBAHS) (concentration: 0.005 M) was used as the electrolyte. A controlled amount of NaOH was added to adjust the pH to 7. For electrochemical exfoliation, a direct current was applied under 10 V for 20 min, during which the system was surrounded by an ice bath to prevent overheating. The intercalated graphene nanosheets were rinsed *via* vacuum filtration with ethanol and deionized water, followed by ultrasonication in DMF for 30 min. The resulting dispersion was centrifuged at 4000 rpm for 10 min to remove unexfoliated crystals.

Ink preparation

To investigate the effect of solvent composition on the surface topography of inkjet-printed MoS_2 films, MoS_2 nanosheets were redispersed in IPA/2-butanol binary solvents that were mixed at volume ratios of 80:20, 85:15, 90:10, and 100:0. MoS_2 channels for back-gated field-effect transistors were printed using MoS_2 dispersion in 100% IPA. For inkjet printing of electrodes, graphene nanosheets were redispersed in ethanol, which exhibits a low boiling point (78.37 °C) and thus promotes rapid solvent evaporation. Specifically, the graphene/DMF dispersion was filtered through a 0.2 μm Nylon (Polymide) membrane (purchased from SciLab) and then the resulting filter cake was bath sonicated in ethanol for 15 min. DMF was added to the graphene/ethanol dispersion (volume ratio of ethanol and DMF = 10:1) to further adjust the rheological properties for stable droplet formation during inkjet printing. The HfS_2 dispersions were used without solvent exchange.

Adjustment of ink concentration

The concentrations of graphene, MoS_2, and HfS_2 inks were first determined using the Beer–Lambert law and the absorption coefficients of each material ($\alpha_{660} = 2460\,L\,g^{-1}\,m^{-1}$ for graphene[30], $\alpha_{672} = 3400\,L\,g^{-1}\,m^{-1}$ for MoS_2[81], and $\alpha_{600} = 13.5\,L\,g^{-1}\,m^{-1}$ for HfS_2[80]) reported in previous studies. After estimating the concentration based on the optical absorbance measured by a UV-visible spectrophotometer (Agilent Technologies, Cary 5000), the inks were diluted to $0.5\,mg\,mL^{-1}$.

Device fabrication

All the printed patterns and devices were fabricated using a drop-on-demand (DoD) inkjet printer (Fujifilm Dimatix, DMP 2850) equipped with 1 and 10 pL cartridges (Fujifilm Dimatix, DMC-11601 and DMC-11610). We used a unipolar waveform with a nozzle voltage of 18 V and a jetting frequency of 2.0 kHz. For MoS_2 and HfS_2 inks, the slew rate and duration were $0.42\,V\,\mu s^{-1}$ and 20.4 μs. Graphene ink was printed with the slew rate and duration of $0.44\,V\,\mu s^{-1}$ and 20.4 μs. Prior to printing, the substrate was rinsed sequentially with acetone, ethanol, and deionized water. All inkjet printing processes were performed at a substrate temperature of 50 °C. For the FETs with vacuum-deposited electrodes, the MoS_2 dot and line patterns were formed on 300-nm SiO_2/Si substrates by applying two printing passes of MoS_2 inks with a drop spacing of 40 μm. The printed films were treated with a bis(trifluoromethane)sulfonimide (TFSI, purchased from Sigma-Aldrich) solution in 1,2-dichloroethane (Fisher Chemical) (concentration: $10\,mg\,mL^{-1}$) at 80 °C for 1 h, followed by annealing at 100 °C for 5 min in an Ar glove box to prevent unintentional doping by adsorbates from the air. Then, the electrodes were created by depositing Cr/Au (5 nm/40 nm) through a photoresist mask patterned with photolithography and lifting off the resist. To fabricate all inkjet-printed FETs, we first formed the dielectric layer by applying eight printing passes of HfS_2 inks with a drop spacing of 20 μm on a heavily doped Si substrate (<0.005 Ω) and anneal the samples at 500 °C for 5 h under ambient conditions for HfO_2 formation. Two printing passes of MoS_2 inks with a drop spacing of 40 μm were then applied to form the channel. After MoS_2 printing, graphene electrodes were printed by applying 30 printing passes of graphene inks with a drop spacing of 60 μm, followed by annealing of the samples at 300 °C for 30 min using a hot plate in an Ar glove box. Finally, the resulting devices were annealed at 200 °C for 30 min in an Ar glove box to improve the adhesion between the gate dielectric, channel, and electrode. For MoS_2 FETs with spin-coated HfO_2 layers, the Si substrate was first treated with oxygen plasma for 5 min. Then, the HfS_2 dispersion was spin-coated four times at 2500 rpm for 40 s and annealed at 500 °C for 5 h under ambient conditions for HfO_2 formation. The MoS_2 channels and graphene electrodes were created following the same procedure used for fabricating all inkjet-printed FETs.

Materials characterization

The thickness and lateral size of the nanosheets and the surface topography of the films were analyzed using an atomic force microscope (Park Systems, Park NX10) under a non-contact mode. Optical microscope and scanning electron microscope (SEM) images were acquired using a metallurgical optical microscope (MICroscope Inc, S39b) and a field-emission scanning electron microscope (JEOL, JSM-7600F), respectively. The cross-sectional image of the device was obtained from a transmission electron microscope (JEOL, JEM-2100F (HR)). Raman and PL spectra were obtained using an Alpho300R spectrometer (WITec) under ambient conditions. Samples were excited with a 532-nm laser source. The signals were collected through a 50× objective lens and dispersed by a diffraction grating (1200 lines mm^{-1} for Raman and 150 lines mm^{-1} for PL). The viscosity and surface tension of the inks were measured using a viscometer (A&D Company, SV-10) and a drop shape analyzer (Krüss, DSA25), respectively. The effective shear rate for the viscosity measurement was $420\,s^{-1}$. Height profiles of the printed graphene electrodes were measured by a surface profilometer (Ambios Technology, Alpha step XP-100). The chemical composition of the HfO_2 was analyzed with x-ray photoelectron spectroscopy (Thermo Fisher Scientific, ESCALAB 250 XI). The areal capacitance of the HfO_2 films was determined based on a metal-insulator-metal structure with gold electrodes.

Device characterization

Current-voltage characteristics were analyzed using a vacuum probe station with a Keithley SCS-4200 system under vacuum ($\sim 10^{-5}$ torr) between 150.15 and 300.15 K for temperature-dependent measurement. All other electrical properties were measured at room temperature under vacuum ($\sim 10^{-5}$ torr). Photoresponsivities at different wavelengths were measured using a Xe lamp coupled to the probe station chamber via an optical fiber. A monochromator was used to obtain the photocurrent at each wavelength. Photoresponsivities under different optical power densities were measured using a 520-nm laser diode.

DATA AVAILABILITY

The data that support the findings of this study are available from the corresponding author upon reasonable request.

REFERENCES

1. Huang, Q. & Zhu, Y. Printing conductive nanomaterials for flexible and stretchable electronics: a review of materials, processes, and applications. *Adv. Mater. Technol.* **4**, 1800546 (2019).
2. Buga, C. S. & Viana, J. C. A review on materials and technologies for organic large-area electronics. *Adv. Mater. Technol.* **6**, 2001016 (2021).
3. Matsui, H., Takeda, Y. & Tokito, S. Flexible and printed organic transistors: from materials to integrated circuits. *Org. Electron.* **75**, 105432 (2019).
4. Gao, M., Li, L. & Song, Y. Inkjet printing wearable electronic devices. *J. Mater. Chem. C* **5**, 2971–2993 (2017).
5. Feng, L., Jiang, C., Ma, H., Guo, X. & Nathan, A. All ink-jet printed low-voltage organic field-effect transistors on flexible substrate. *Org. Electron.* **38**, 186–192 (2016).
6. Fang, Y. et al. Inkjet-printed vertical organic field-effect transistor arrays and their image sensors. *ACS Appl. Mater. Interfaces* **10**, 30587–30595 (2018).
7. Zhou, L. et al. Inkjet-printed small-molecule organic light-emitting diodes: halogen-free inks, printing optimization, and large-area patterning. *ACS Appl. Mater. Interfaces* **9**, 40533–40540 (2017).
8. Zhao, J. et al. High-speed fabrication of all-inkjet-printed organometallic halide perovskite light-emitting diodes on elastic substrates. *Adv. Mater.* **33**, 2102095 (2021).
9. Jung, S. et al. All-inkjet-printed, all-air-processed solar cells. *Adv. Energy Mater.* **4**, 1400432 (2014).
10. Tang, W. et al. Recent progress in printable organic field effect transistors. *J. Mater. Chem. C* **7**, 790–808 (2019).
11. Scheideler, W. J., Kumar, R., Zeumault, A. R. & Subramanian, V. Low-temperature-processed printed metal oxide transistors based on pure aqueous inks. *Adv. Funct. Mater.* **27**, 1606062 (2017).
12. Chung, S., Cho, K. & Lee, T. Recent progress in inkjet-printed thin-film transistors. *Adv. Sci.* **6**, 1801445 (2019).
13. Everaerts, K. et al. Printed indium gallium zinc oxide transistors. Self-assembled nanodielectric effects on low-temperature combustion growth and carrier mobility. *ACS Appl. Mater. Interfaces* **5**, 11884–11893 (2013).
14. Li, Y. et al. All inkjet-printed metal-oxide thin-film transistor array with good stability and uniformity using surface-energy patterns. *ACS Appl. Mater. Interfaces* **9**, 8194–8200 (2017).
15. Scheideler, W. J., McPhail, M. W., Kumar, R., Smith, J. & Subramanian, V. Scalable, high-performance printed InOx transistors enabled by ultraviolet-annealed printed high-*k* AlOx gate dielectrics. *ACS Appl. Mater. Interfaces* **10**, 37277–37286 (2018).
16. Shao, S. et al. Large-area (64 × 64 Array) inkjet-printed high-performance metal oxide bilayer heterojunction thin film transistors and *n*-metal-oxide-semiconductor (NMOS) inverters. *J. Mater. Sci. Technol.* **81**, 26–35 (2021).
17. Kim, S. Y. et al. High-resolution electrohydrodynamic inkjet printing of stretchable metal oxide semiconductor transistors with high performance. *Nanoscale* **8**, 17113–17121 (2016).
18. Datta, R. S. et al. Flexible two-dimensional indium tin oxide fabricated using a liquid metal printing technique. *Nat. Electron.* **3**, 51–58 (2020).
19. Tang, Y., Huang, C.-H. & Nomura, K. Vacuum-free liquid-metal-printed 2D indium–tin oxide thin-film transistor for oxide inverters. *ACS Nano* **16**, 3280–3289 (2022).
20. Hamlin, A. B., Ye, Y., Huddy, J. E., Rahman, M. S. & Scheideler, W. J. 2D transistors rapidly printed from the crystalline oxide skin of molten indium. *npj 2D Mater. Appl.* **6**, 16 (2022).
21. Dolzhnikov Dmitriy, S. et al. Composition-matched molecular "solders" for semiconductors. *Science* **347**, 425–428 (2015).
22. Choi, J.-H. et al. Bandlike transport in strongly coupled and doped quantum dot solids: a route to high-performance thin-film electronics. *Nano Lett.* **12**, 2631–2638 (2012).
23. Lu, S. & Franklin, A. D. Printed carbon nanotube thin-film transistors: progress on printable materials and the path to applications. *Nanoscale* **12**, 23371–23390 (2020).
24. Bucella, S. G. et al. Inkjet printed single-walled carbon nanotube based ambipolar and unipolar transistors for high-performance complementary logic circuits. *Adv. Electron. Mater.* **2**, 1600094 (2016).
25. Aigner, W. et al. Intra- and inter-nanocrystal charge transport in nanocrystal films. *Nanoscale* **10**, 8042–8057 (2018).
26. Zorn, N. F. & Zaumseil, J. Charge transport in semiconducting carbon nanotube networks. *Appl. Phys. Rev.* **8**, 041318 (2021).
27. Lin, Z., Huang, Y. & Duan, X. Van der Waals thin-film electronics. *Nat. Electron.* **2**, 378–388 (2019).
28. Hu, G. et al. Functional inks and printing of two-dimensional materials. *Chem. Soc. Rev.* **47**, 3265–3300 (2018).
29. Lin, Z. et al. Solution-processable 2D semiconductors for high-performance large-area electronics. *Nature* **562**, 254–258 (2018).
30. Hernandez, Y. et al. High-yield production of graphene by liquid-phase exfoliation of graphite. *Nat. Nanotechnol.* **3**, 563–568 (2008).
31. Green, A. A. & Hersam, M. C. Solution phase production of graphene with controlled thickness via density differentiation. *Nano Lett.* **9**, 4031–4036 (2009).
32. Secor, E. B., Prabhumirashi, P. L., Puntambekar, K., Geier, M. L. & Hersam, M. C. Inkjet printing of high conductivity, flexible graphene patterns. *J. Phys. Chem. Lett.* **4**, 1347–1351 (2013).
33. Kang, J. et al. Thickness sorting of two-dimensional transition metal dichalcogenides via copolymer-assisted density gradient ultracentrifugation. *Nat. Commun.* **5**, 5478 (2014).
34. Zhu, J. et al. Solution-processed dielectrics based on thickness-sorted two-dimensional hexagonal boron nitride nanosheets. *Nano Lett.* **15**, 7029–7036 (2015).
35. Shen, J. et al. Liquid phase exfoliation of two-dimensional materials by directly probing and matching surface tension components. *Nano Lett.* **15**, 5449–5454 (2015).
36. Li, J., Naiini, M. M., Vaziri, S., Lemme, M. C. & Östling, M. Inkjet printing of MoS₂. *Adv. Funct. Mater.* **24**, 6524–6531 (2014).
37. Seo, J.-W. T. et al. Fully inkjet-printed, mechanically flexible MoS₂ nanosheet photodetectors. *ACS Appl. Mater. Interfaces* **11**, 5675–5681 (2019).
38. Kelly Adam, G. et al. All-printed thin-film transistors from networks of liquid-exfoliated nanosheets. *Science* **356**, 69–73 (2017).
39. Kelly A. G., O'Suilleabhain D., Gabbett C. & Coleman J. N. The electrical conductivity of solution-processed nanosheet networks. *Nat. Rev. Mater.* **7**, 217–234 (2021).
40. Hossain, R. F. & Kaul, A. B. Inkjet-printed MoS₂-based field-effect transistors with graphene and hexagonal boron nitride inks. *J. Vac. Sci. Technol. B* **38**, 042206 (2020).
41. Carey, T. et al. Inkjet printed circuits with 2D semiconductor inks for high-performance electronics. *Adv. Electron. Mater.* **7**, 2100112 (2021).
42. Piatti, E. et al. Charge transport mechanisms in inkjet-printed thin-film transistors based on two-dimensional materials. *Nat. Electron.* **4**, 893–905 (2021).
43. Radisavljevic, B., Radenovic, A., Brivio, J., Giacometti, V. & Kis, A. Single-layer MoS₂ transistors. *Nat. Nanotechnol.* **6**, 147–150 (2011).
44. Guo, Z. et al. High-performance polarization-sensitive photodetectors on two-dimensional β-InSe. *Natl. Sci. Rev.* **9**, nwab098 (2021).
45. Qiao, H. et al. Self-powered photodetectors based on 2D materials. *Adv. Opt. Mater.* **8**, 1900765 (2020).
46. Fan, T., Xie, Z., Huang, W., Li, Z. & Zhang, H. Two-dimensional non-layered selenium nanoflakes: facile fabrications and applications for self-powered photodetector. *Nanotechnology* **30**, 114002 (2019).
47. Zhang, Y. et al. Graphdiyne-based flexible photodetectors with high responsivity and detectivity. *Adv. Mater.* **32**, 2001082 (2020).
48. Yin, Z. et al. Single-layer MoS₂ phototransistors. *ACS Nano* **6**, 74–80 (2012).
49. Wang, B. et al. High-*k* gate dielectrics for emerging flexible and stretchable electronics. *Chem. Rev.* **118**, 5690–5754 (2018).
50. Zeumault, A. & Subramanian, V. Mobility enhancement in solution-processed transparent conductive oxide TFTs due to electron donation from traps in high-*k* gate dielectrics. *Adv. Funct. Mater.* **26**, 955–963 (2016).
51. Carey, T. et al. Fully inkjet-printed two-dimensional material field-effect heterojunctions for wearable and textile electronics. *Nat. Commun.* **8**, 1202 (2017).
52. Worsley, R. et al. All-2D material inkjet-printed capacitors: toward fully printed integrated circuits. *ACS Nano* **13**, 54–60 (2019).

53. Joseph, A. M., Nagendra, B., Bhoje Gowd, E. & Surendran, K. P. Screen-printable electronic ink of ultrathin boron nitride nanosheets. *ACS Omega* **1**, 1220–1228 (2016).

54. Gupta, B. & Matte, H. S. S. R. Solution-processed layered hexagonal boron nitride dielectrics: a route toward fabrication of high performance flexible devices. *ACS Appl. Electron. Mater.* **1**, 2130–2139 (2019).

55. Knobloch, T. et al. The performance limits of hexagonal boron nitride as an insulator for scaled CMOS devices based on two-dimensional materials. *Nat. Electron.* **4**, 98–108 (2021).

56. Azadmanjiri, J. et al. A review on hybrid nanolaminate materials synthesized by deposition techniques for energy storage applications. *J. Mater. Chem. A* **2**, 3695–3708 (2014).

57. Splendiani, A. et al. Emerging photoluminescence in monolayer MoS_2. *Nano Lett.* **10**, 1271–1275 (2010).

58. Hoath, S. D. *Fundamentals of Inkjet Printing: The Science of Inkjet and Droplets* (John Wiley & Sons, 2016).

59. Wan, X. et al. In situ ultrafast and patterned growth of transition metal dichalcogenides from inkjet-printed aqueous precursors. *Adv. Mater.* **33**, 2100260 (2021).

60. McManus, D. et al. Water-based and biocompatible 2D crystal inks for all-inkjet-printed heterostructures. *Nat. Nanotechnol.* **12**, 343–350 (2017).

61. Finn, D. J. et al. Inkjet deposition of liquid-exfoliated graphene and MoS_2 nanosheets for printed device applications. *J. Mater. Chem. C.* **2**, 925–932 (2014).

62. Torrisi, F. et al. Inkjet-printed graphene electronics. *ACS Nano* **6**, 2992–3006 (2012).

63. Golovynskyi, S. et al. Exciton and trion in few-layer MoS_2: thickness- and temperature-dependent photoluminescence. *Appl. Surf. Sci.* **515**, 146033 (2020).

64. Deegan, R. D. et al. Capillary flow as the cause of ring stains from dried liquid drops. *Nature* **389**, 827–829 (1997).

65. Mampallil, D. & Eral, H. B. A review on suppression and utilization of the coffee-ring effect. *Adv. Colloid Interface Sci.* **252**, 38–54 (2018).

66. Hu, G. et al. A general ink formulation of 2D crystals for wafer-scale inkjet printing. *Sci. Adv.* **6**, eaba5029 (2020).

67. He, P. & Derby, B. Controlling coffee ring formation during drying of inkjet printed 2D inks. *Adv. Mater. Interfaces* **4**, 1700944 (2017).

68. Kim, H. et al. Sheet size-induced evaporation behaviors of inkjet-printed graphene oxide for printed electronics. *ACS Appl. Mater. Interfaces* **8**, 3193–3199 (2016).

69. Amani, M. et al. Near-unity photoluminescence quantum yield in MoS_2. *Science* **350**, 1065–1068 (2015).

70. Xue, J., Huang, S., Wang, J.-Y. & Xu, H. Q. Mott variable-range hopping transport in a MoS_2 nanoflake. *RSC Adv.* **9**, 17885–17890 (2019).

71. Raj, K. G. & Joy, P. A. Cross over from 3D variable range hopping to the 2D weak localization conduction mechanism in disordered carbon with the extent of graphitization. *Phys. Chem. Chem. Phys.* **17**, 16178–16185 (2015).

72. Zhao, Z.-Y. & Liu, Q.-L. Study of the layer-dependent properties of MoS_2 nanosheets with different crystal structures by DFT calculations. *Catal. Sci. Technol.* **8**, 1867–1879 (2018).

73. Zhao, Q. et al. The role of traps in the photocurrent generation mechanism in thin InSe photodetectors. *Mater. Horiz.* **7**, 252–262 (2020).

74. Li, L. et al. Few-layered PtS_2 phototransistor on h-BN with high gain. *Adv. Funct. Mater.* **27**, 1701011 (2017).

75. Furchi, M. M., Polyushkin, D. K., Pospischil, A. & Mueller, T. Mechanisms of photoconductivity in atomically thin MoS_2. *Nano Lett.* **14**, 6165–6170 (2014).

76. Lopez-Sanchez, O., Lembke, D., Kayci, M., Radenovic, A. & Kis, A. Ultrasensitive photodetectors based on monolayer MoS_2. *Nat. Nanotechnol.* **8**, 497–501 (2013).

77. Wang, X. et al. Ultrasensitive and broadband MoS_2 photodetector driven by ferroelectrics. *Adv. Mater.* **27**, 6575–6581 (2015).

78. Kelly, A. G., Finn, D., Harvey, A., Hallam, T. & Coleman, J. N. All-printed capacitors from graphene-BN-graphene nanosheet heterostructures. *Appl. Phys. Lett.* **109**, 023107 (2016).

79. Abdolhosseinzadeh, S. et al. A universal approach for room-temperature printing and coating of 2D materials. *Adv. Mater.* **34**, 2103660 (2022).

80. Kim, J. et al. All-solution-processed van der Waals heterostructures for wafer-scale electronics. *Adv. Mater.* **32**, 2106110 (2022).

81. Coleman, J. N. et al. Two-dimensional nanosheets produced by liquid exfoliation of layered materials. *Science* **331**, 568–571 (2011).

ACKNOWLEDGEMENTS

AUTHOR CONTRIBUTIONS

O.S., D.R., and Jo.K. conceived the idea and designed all the experiments. O.S., Ji.K., and Y.J. optimized the solution processing. V.M., A.S., and Z.S. synthesized the layered crystals. O.S. and Y.-H.K. pursued inkjet printing. Y.A.K. and J.H.C. analyzed the dielectric properties. Jo.K. supervised the entire project. All authors wrote the manuscript and discussed the results at all stages.

COMPETING INTERESTS

The authors declare no competing interests.

ADDITIONAL INFORMATION

Supplementary information The online version contains supplementary material available at https://doi.org/10.1038/s41699-022-00337-1.

Correspondence and requests for materials should be addressed to Joohoon Kang.

Reprints and permission information is available at http://www.nature.com/reprints

Publisher's note Springer Nature remains neutral with regard to jurisdictional claims in published maps and institutional affiliations.